

ARTICLE

<https://doi.org/10.1038/s42005-018-0095-3>

OPEN

Brilliant gamma-ray beam and electron-positron pair production by enhanced attosecond pulses

Yan-Jun Gu^{1,2}, Ondrej Klimo^{1,3}, Sergei V. Bulanov^{1,4,5} & Stefan Weber¹

Electron-positron pair production via Breit-Wheeler process requires laser intensities approaching 10^{24} W cm⁻² due to the small cross-section. Here, we propose a mechanism for brilliant γ -ray emission and dense GeV pairs creation accompanied with high-harmonic generation by using plasma mirror and an ultra short pulse with the intensity of 3×10^{23} W cm⁻². The laser is reflected by the solid surface after propagating tens of microns in a near-critical density plasma and breaks into short wave packets. The intensity of the reflected high order harmonic field is enhanced by the focusing and compression effects from the deformed oscillating mirror. The radiation trapped electrons emit γ -photons while colliding with the reflected attosecond pulses. The peak intensity of the γ -ray reaches 0.74 PW with the brilliance of 2×10^{24} s⁻¹ mm⁻² mrad⁻² (0.1%BW)⁻¹ (at 58 MeV). A GeV positron beam is obtained with density of 4×10^{21} cm⁻³ and a particle number of 5.6×10^9 .

¹Institute of Physics of the ASCR, ELI-Beamlines, Na Slovance 2, 18221 Prague, Czech Republic. ²Institute of Plasma Physics of the CAS, Za Slovankou 1782/3, 18200 Prague, Czech Republic. ³FNSPE, Czech Technical University in Prague, 11519 Prague, Czech Republic. ⁴Kansai Photon Science Institute, National Institutes for Quantum and Radiological Science and Technology, 8-1-7 Umemidai, Kizugawa-shi, Kyoto 619-0215, Japan. ⁵A. M. Prokhorov Institute of General Physics of the Russian Academy of Sciences, Vavilova 38, 119991 Moscow, Russia. Correspondence and requests for materials should be addressed to Y.-J.G. (email: yanjun.gu@eli-beams.eu)

The rapid development of laser technology allowed for significant increase of the pulse power and intensity. The state-of-the-art laser facilities are able to exceed the intensity level of $10^{22} \text{ W cm}^{-2}$. The next generation 10-PW installations are expected to reach $10^{23-24} \text{ W cm}^{-2}$ or even higher^{3,4}. At such intensities, the laser-plasma interaction approaches the radiation-dominated quantum electrodynamics (QED) regime. A relativistic electron absorbs the energy from the electromagnetic (EM) field and emits high-energy photons at the same time. The radiation friction effect is dominant when the rate of radiation emission overcomes the rate of absorption. When the emitted photon energy is of the order of the electron energy, QED effects become important. Novel physical processes such as gamma-photon emission, electron-positron pair creation and QED-cascade come into play under these extreme intensity conditions. The abundant new phenomena provide possibilities of studying high-energy density physics, laboratory astrophysics, and to address the fundamental physics in QED⁵⁻⁸.

Among the large number of new topics, γ -ray emission and e^+e^- pair creation in laser-plasma interactions have been studied extensively in recent years⁹⁻²⁷. γ -ray generation by Bremsstrahlung radiation has been demonstrated in laser-solid interactions^{28,29}. γ -photons in the giant-dipole-resonance range are obtained via Bremsstrahlung of electron bunches³⁰. A γ -ray beam with the brilliance of $10^{20} \text{ s}^{-1} \text{ mm}^{-2} \text{ mrad}^{-2} (0.1\% \text{ BW})^{-1}$ is obtained in experiment from nonlinear relativistic Thomson scattering³¹. Multi-MeV photons are also emitted by an ultra-relativistic electron beam in a self-generated magnetic field³². The energy transfer efficiency from laser to the photons is about 1.45%. One of the main mechanisms for γ ray production is the nonlinear Compton scattering^{33,34}, in which the relativistic electrons interact with the strong EM field. Recently Chang et al.²³ proposed high-brightness photon bunch generation by circularly polarized laser pulses. In ref³⁵, high brilliance ($10^{25} \text{ s}^{-1} \text{ mm}^{-2} \text{ mrad}^{-2} (0.1\% \text{ BW})^{-1}$) and collimated γ -ray flashes are obtained from plasma filaments based on the synchrotron emission of a high density ultra-relativistic electron beam. The γ -rays from harmonically resonant betatron oscillation in a plasma wake is obtained in experiments with the brilliance of $10^{23} \text{ s}^{-1} \text{ mm}^{-2} \text{ mrad}^{-2} (0.1\% \text{ BW})^{-1}$ ³⁶. The gamma-ray pulses with similar brilliance were obtained recently by using a Laguerre-Gaussian mode laser and compound targets³⁷. High-energy photons are related to e^+e^- pair creation at extreme high laser intensity via the multiphoton Breit-Wheeler (BW) process^{38,39}, $\gamma + n\hbar\omega_0 \rightarrow e^- + e^+$, here ω_0 is the laser frequency. In general, the BW process requires a laser intensity as high as $10^{24} \text{ W cm}^{-2}$ ²¹⁰. Multiple counter-propagating pulses have been employed to achieve pair creation at laser intensities of the order of $10^{23} \text{ W cm}^{-2}$ ^{212,22,24}. With even higher laser intensities as $10^{23-25} \text{ W cm}^{-2}$, QED cascades are obtained⁴⁰⁻⁴². In ref⁴², about 1.44×10^7 photons are emitted and $5.5 \times 10^4 e^+e^-$ are obtained as a result of a QED cascade. Our previous work proposed a mechanism for pair creation by a single laser pulse interacting with near-critical-density (NCD) plasmas²¹. The longitudinal self-injected electrons collide with the EM field in a regime characterized by a large cross-section for γ -ray emission and e^+e^- production. In our recent work⁴³, a mechanism to generate a tunable γ -ray beam by using a plasma mirror was reported. The laser-wakefield acceleration regime is used which provides the controllable high-energy electron beam. The corresponding γ -ray beam is emitted by the electron beam via nonlinear Compton scattering. Since the beam quality of the wakefield accelerated electrons is scalable, the quality of the emitted photons is also under control. In the present paper, we propose a mechanism of bright γ -ray emission and positron acceleration by using ultra-intense attosecond pulses colliding with a relativistic electron bunch accelerated directly by the laser-field via the $\mathbf{j} \times \mathbf{B}$ heating effect. The attosecond pulses are generated by the

relativistic oscillating mirror localized at the end of the NCD target. The plasma mirror not only reflects the laser field but also enhances the intensity due to the significant deformation of the surface. The reflected field is enhanced by both compression and focusing effect. The concave mirror can provide an intensity more than two times higher than the incident one. With the laser intensity of $3 \times 10^{23} \text{ W cm}^{-2}$, a brilliant γ ray pulse with brilliance of $2 \times 10^{24} \text{ s}^{-1} \text{ mm}^{-2} \text{ mrad}^{-2} (0.1\% \text{ BW})^{-1}$ (at 58 MeV) and a GeV positron beam with the density of $4 \times 10^{21} \text{ cm}^{-3}$ are obtained with three dimensional particle-in-cell simulations. Compared with the proposed regimes in refs^{30,31,36}, the energy of the γ -photons is much higher in our case. The energy transfer efficiency in the proposed mechanism is comparable to the previous ones³². The brilliance of the γ ray is similar to the highest achieved in ref³⁵. The number of the generated positrons is comparable with the previous work, in which two counter-propagating ultra-intense laser pulses are used¹⁹. However, the energy of the obtained positrons is much higher in our case due to the further acceleration of the positrons by the reflected laser field. The whole process can be divided into three stages: relativistic electron trapping and acceleration in the laser field, high-harmonics generation by relativistic oscillating mirror and γ ray and e^+e^- pair creation by the reflected attosecond pulse.

Results

Simulation setup. The laser pulse is linear polarized and propagates along the x-direction. It's focused on the target with the peak intensity of $3 \times 10^{23} \text{ W cm}^{-2}$. The pulse has a Gaussian temporal profile with a duration (full width at half maximum (FWHM)) of $\tau = 15 \text{ fs}$ of the field amplitude and a transversely Gaussian distribution $a = a_0 \exp(-r^2/\sigma^2)$, where $\sigma = r_0 / (2\sqrt{\ln 2})$. It is cut at $2 \times \tau$ from the peak intensity, which means the peak intensity locates at $x = -2c\tau$ at $t = 0$. The cut-off intensity is $\sim 10^{14} \text{ W cm}^{-2}$. The dimensionless amplitude of the laser pulse is $a_0 = eE_0/m_e\omega_0c \approx 468$, where ω_0 is the laser frequency, e and m_e are the electron charge and mass, respectively; and c is the speed of light in vacuum. $E_0 = \sqrt{8\pi I_0/c}$ is the laser electric field strength. The focus spot size (FWHM) of the laser is $r_0 = 3 \lambda$, where $\lambda = 1 \mu\text{m}$ is the laser wavelength. The laser radiation interacts with a double-layer target. The first layer consists of a hydrogen plasma with the peak density of $n_0 = 4n_c$, where $n_c = m_e\omega^2/4\pi e^2$ is the plasma critical density. Its thickness is 22λ . The second layer is at the end of the hydrogen plasma target. It is a pre-ionized gold layer (Au^{51+}) with the density of $600n_c$ and of the thickness of 1λ . The details of the simulations and the code information are presented in the Methods.

Relativistic electron acceleration in the laser field. The laser power employed in the simulation is above the critical power for the self-focusing⁴⁴, $P > P_{cn}/n_0$ ($P_c = 2m_e^2c^5/e^2 = 17\text{GW}$), and satisfies the relativistic self-channeling condition⁴⁵. Electrons are trapped inside the plasma channel due to radiation friction when the critical laser amplitude is approaching $a_{\text{rad}} \approx (4\pi r_e/3\lambda)^{-1/3} \sim 400$, where $r_e = e^2/m_e c^2$ is the classical electron radius. Instead of being scattered transversely, the electrons are confined in the laser field when the transverse radiation reaction force is comparable to the expelling ponderomotive force. On the other hand, the electrons drift slowly backwards inside the pulse being accelerated by the laser field to high energy as discussed in ref. ²¹. The electron density distribution at $t = 33T_0$ is shown in Fig. 1a. The density of the trapped electrons modulates with the scale length corresponding to the laser intensity profile (the black curve). The kinetic energy of the electrons is above 1 GeV as shown by the scatter diagram. The main mechanism of electron acceleration comes from the component of the $\mathbf{j} \times \mathbf{B}$ force. The

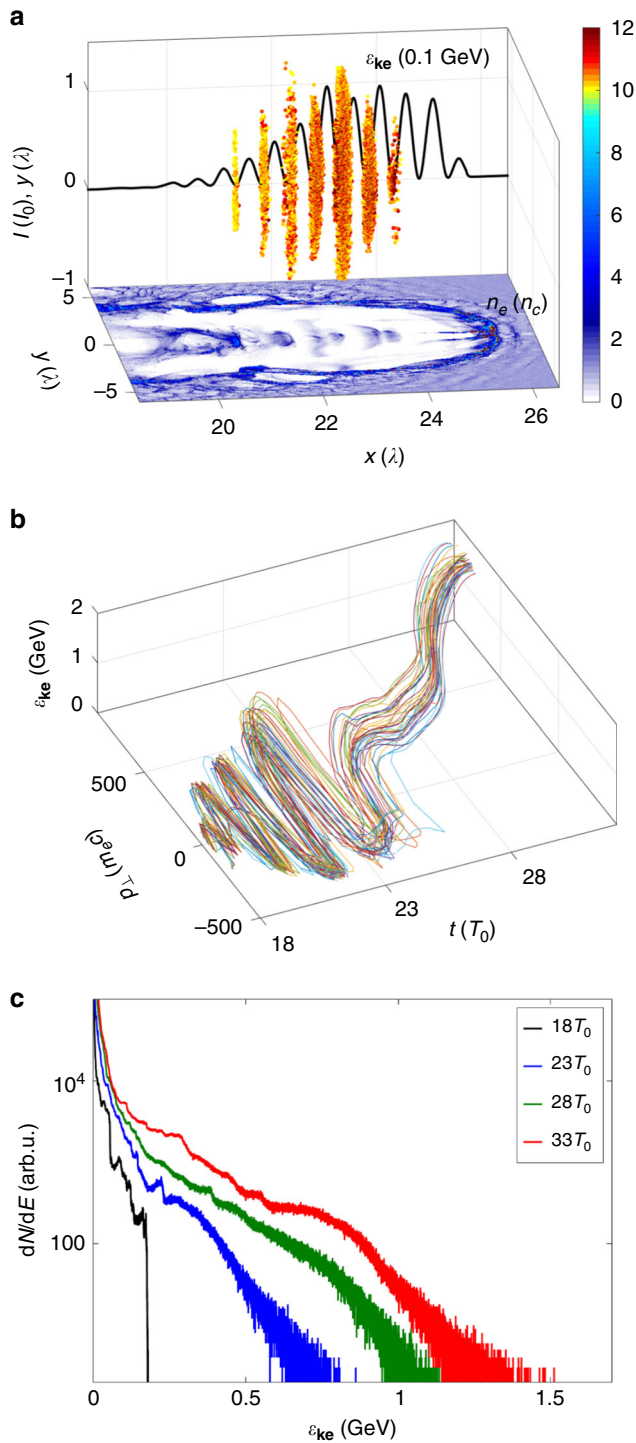


Fig. 1 Electron acceleration effect. **a** The electron density distribution at $33T_0$ is projected on the bottom plane. The profile of laser intensity along the laser axis ($y = 0$) is plotted by the black line. The vertical axis shows the amplitude of the intensity and also the coordinates in the y -direction. The scatter diagram includes the radiation trapped high energy electrons. The colorbar represents the density (normalized to critical density) and the kinetic energy (normalized to 0.1 GeV). **b** The evolution of transverse momentum (p_{\perp}) and kinetic energy (ϵ_{ke}) of the traced high energy electrons. **c** The electron energy spectrum at time equals $18T_0$, $23T_0$, $28T_0$, and $33T_0$.

electrons trapped in the laser pulse experience a strong EM field in the transverse directions and obtain large transverse momentum. Figure 1b shows the evolution of the transverse momentum and kinetic energy of the traced electrons randomly selected from the trapped high energy electrons. After several oscillation periods, the transverse momentum p_{\perp} grows to hundreds of $m_e c$. Under the ultra-relativistic conditions, the electron velocity is close to the speed of light and then the magnetic field force is as strong as the electric field force. The $\mathbf{j} \times \mathbf{B}$ force converts the transverse momentum to the longitudinal direction and accelerates the electrons to high energy in a short distance. Although the radiation reaction suppresses the $\mathbf{j} \times \mathbf{B}$ heating due to the momentum loss for photon emission, the electron bunch can still be accelerated to values above GeV. The corresponding electron spectrum is shown in Fig. 1c.

High-energy electrons interacting with a strong EM field emit photons via the nonlinear Compton scattering. The Lorentz and gauge invariant parameter $\chi_e = \sqrt{(F^{\mu\nu} p_{\nu})^2} / (E_s m_e c)^{39}$ characterizes the probability of the photon emission, where $F_{\mu\nu} = \partial_{\mu} A_{\nu} - \partial_{\nu} A_{\mu}$ is the four-tensor of the EM field, p_{ν} is the electron four-momentum and $E_s = m_e^2 c^3 / e \hbar$ is the critical QED electric field⁴⁶. It can be expressed as $\chi_e = (E/E_s)(\gamma - p_x/m_e c)$ in the case of a plane EM wave propagating in x -direction. In the ultra-relativistic limit, $\gamma \gg 1$, the photon emission probability is maximized in a counter-propagating geometry of the electrons and EM field, $\chi_e^{\uparrow} \simeq 2\gamma(E/E_s)$. In contrast, it decreases to $\chi_e^{\downarrow} \simeq (2\gamma)^{-1}(E/E_s)$ for the co-propagating electrons. Figure 2a presents the electron energy and angular distribution at $33T_0$. The energy of the electrons, normalized to GeV, is scaled by the radius. The accelerated electrons are mainly forward propagating, i.e., co-propagating with the laser field, with small opening angle. Therefore, the γ -ray emission at this stage is suppressed due to the small χ_e . The characteristic radiation energy is estimated as $\hbar\omega_{\gamma} \sim 2a_0^3 \hbar\omega_L \approx 200 \text{ MeV}$ ⁴⁷. Both the number and the energy of the emitted photon are relatively low as can be seen in Fig. 2b. At this stage, the γ -photon emission is similar to the electron beam synchrotron radiation in the near-critical density plasma as proposed in refs. 48,49, in which the resonant electrons accelerated directly by the laser field in the plasma channel dominate the radiation process in the forward direction.

High-order harmonics generation by relativistic oscillating mirror.

At the rear end of the hydrogen plasma layer, a solid target is attached to provide efficient reflection of the laser pulse. To block the transmission, the target is set to be pre-ionized Au⁵¹⁺ with an electron density of $600n_c$ and a thickness of 1λ . The target is fully opaque even under the relativistic transparency condition and reflects the incident light as a mirror. Figure 3a, b shows the evolution of the electron and ion density distributions (transversely averaged in $-0.5 < y(\lambda) < 0.5$) of the solid target. The initial interface between the hydrogen plasma layer and the solid target is located at $x = 32\lambda$. The electrons on the surface are pushed inward by the laser field. However, the ions with much heavier mass respond in a longer time scale. Similar to the laser piston model⁵⁰, a double-layer structure with separated electrons and ions is formed. According to the balance between the momentum flux of the radiation and those of the charged particles, one can obtain the relationship between the piston velocity, the laser intensity and the target density: $I / [(m_i/Z_i + m_e)n_e c^3] (1 - \beta_f)(1 + \beta_f) = \gamma_f^2 \beta_f^2$, in which β_f is the normalized piston

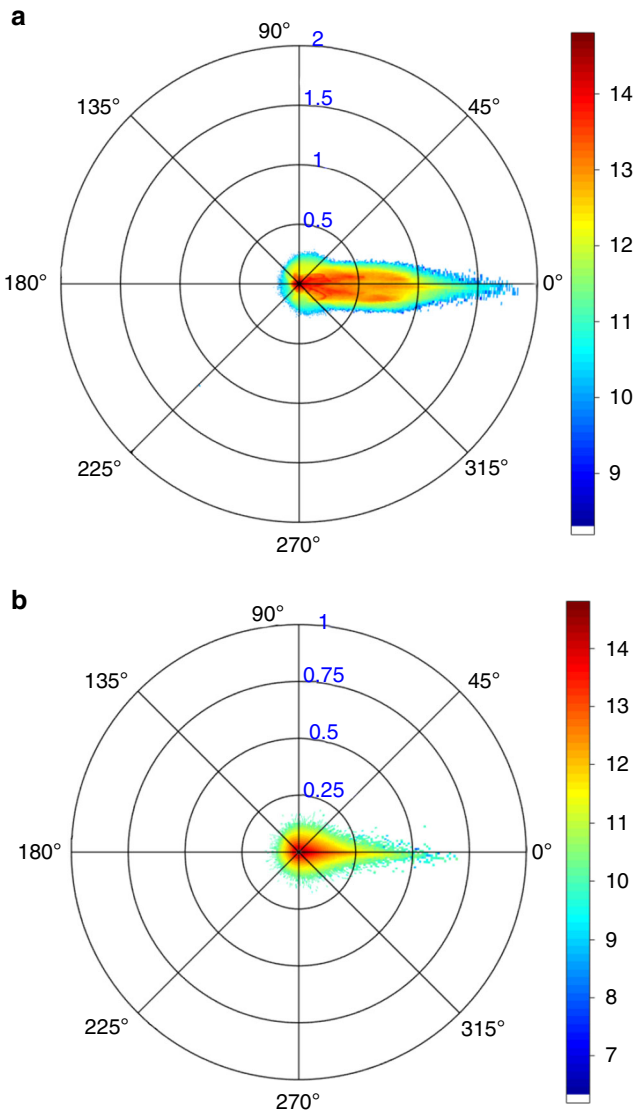


Fig. 2 Electron and photon in early stage. The angular-energy distribution of electrons and photons at $33T_0$ are shown in frames **a**, **b**, respectively. The radial distance is the energy in GeV. The colorbar shows the particle number in logarithmic scale with arbitrary unit

velocity, $\gamma_f = (1 - \beta_f^2)^{-1/2}$ is the Lorentz factor, Z_i is the ion charge state and n_e is the electron density on the surface. The obtained normalized target surface velocity, $\beta_f \sim 0.14c$, is plotted by the dashed line in Fig. 3b. For the time interval of the pulse duration (15fs), this is well consistent with the forward moving velocity of the ion density surface. The electrons are forced back to the ion layer by the strong charge separation field generated by the unbalanced double-layer structure. The resulting electron oscillations can be seen from the electron density surface modulations in Fig. 3a. The critical electron surface oscillates around the ion layer. Since the incident laser pulse is reflected by the critical density surface, the solid gold layer behaves as an oscillating mirror.

The model of relativistic oscillating mirror and attosecond second generation have been proposed and discussed in refs. ⁵¹⁻⁵⁴. The frequency of the reflected laser field is blue shifted since the incident pulse experiences the Doppler effect and the incident pulse also breaks up into short-wave packets⁵⁵. The intensity

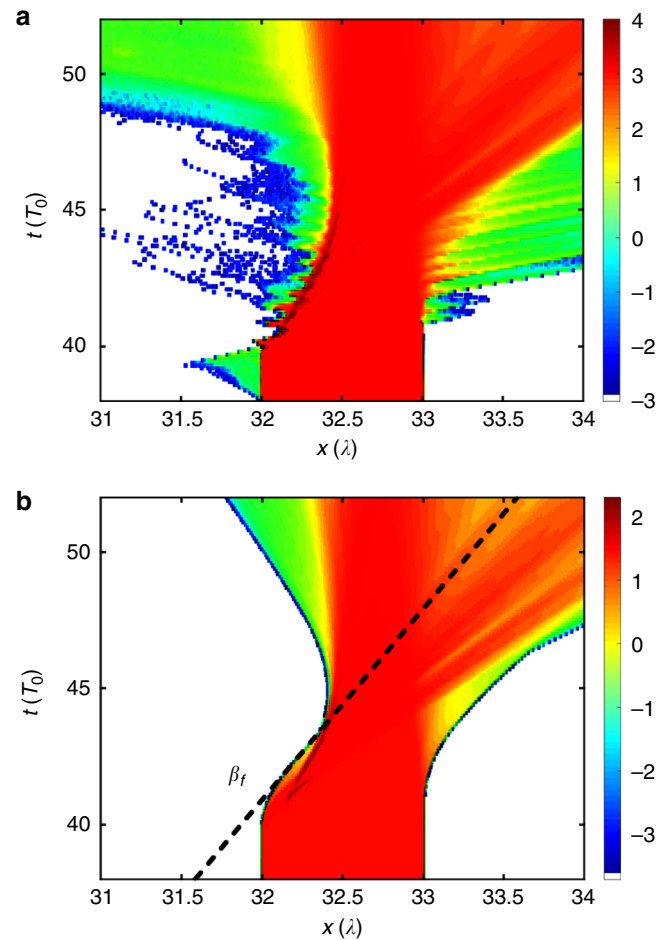


Fig. 3 Surface of the oscillating plasma mirror. The evolutions of the electron and ion density (transversely averaged in $-0.5 < y(\lambda) < 0.5$) of the solid target are shown in **a**, **b**. The black dashed line in **b** indicates the piston velocity β_f . The colorbars in **a**, **b** represent $\log_{10}(n_e/n_c)$ and $\log_{10}(n_i/n_c)$, respectively

distribution of the reflected laser field at $52T_0$ in the x,y -plane is shown in Fig. 4a. The solid red line represents the Poynting vector profile along the laser axis, in which the negative value indicates the backward propagation. It is seen that the reflected radiation breaks into several ultra short spikes. The profile of the intensity on laser axis shows that the duration of the spike (FWHM) is about 200 attoseconds. The intensity of the reflected pulse increases by a factor of two with a smaller spot size of about 0.85λ , as shown by the black line corresponding to the profile of the laser intensity along the maximum intensity at $x = 20.9\lambda$. The increase of intensity and the reduction of the spot size are due to the focusing effect produced by the deformed solid target. The electron density distribution of the solid target at $t = 44T_0$ is plotted in Fig. 4b. The reflecting surface is deformed inward as a concave mirror focusing the reflected light. The black arrows represent the Poynting vectors of the reflected field, which are focused so that the intensity increases. Limited by the slight curvature, the reflected field cannot be tightly focused within several wavelengths. The focal length can be estimated from the laser radius r_0 and the maximum displacement of the solid surface as: $c\beta_f\tau \approx 0.56\lambda$. This gives for the focal length the value of $f \approx [r_0^2 + (c\beta_f\tau)^2] / 4(c\beta_f\tau) \approx r_0^2 / (4c\beta_f\tau)\lambda$. Comparing the intensity profiles in Fig. 4a, b, one finds that it requires about

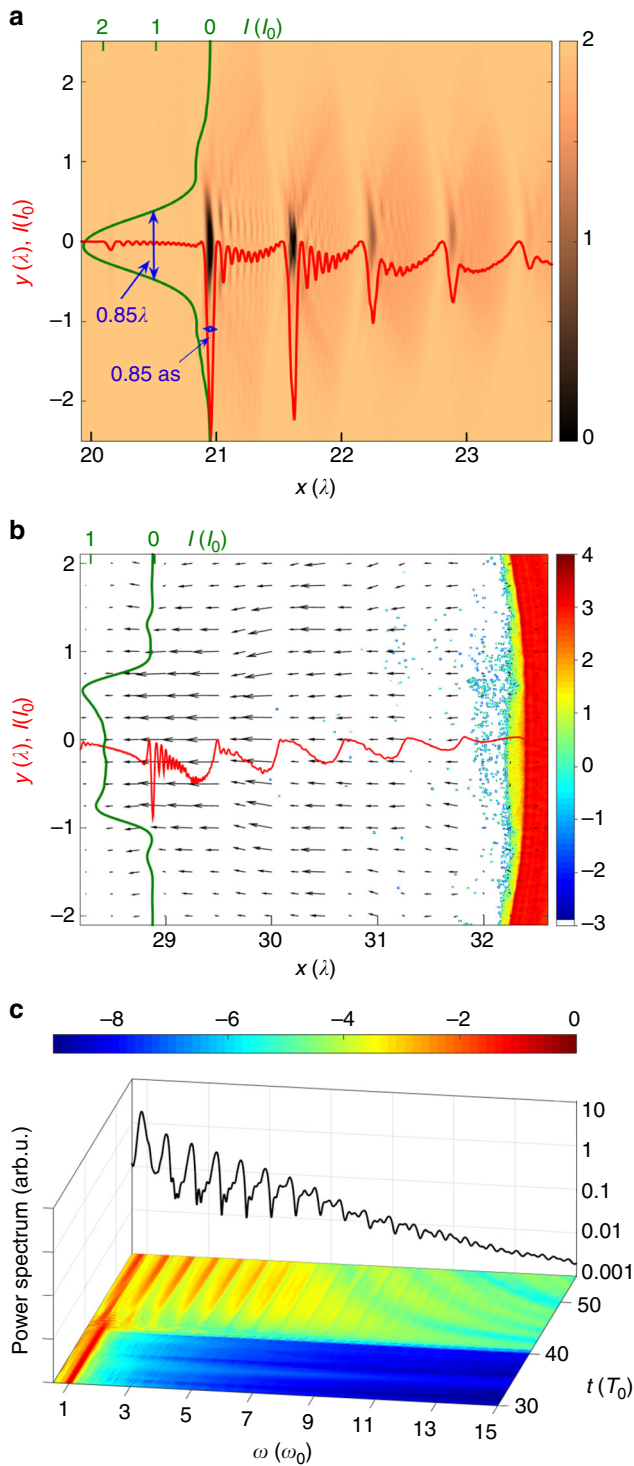


Fig. 4 Reflected high-order harmonic field. **a** Reflected intensity distribution at $t = 52T_0$. The red line is the Poynting vector profile along the laser axis ($y = 0$). The green line (related to the upper axis) is the intensity profile along $x = 20.9\lambda$, which is corresponding to the maximum of the intensity. The colorbar shows the intensity normalized to the initial peak intensity I_0 . **b** The electron density distribution of the solid target at $t = 44T_0$. The black arrows represent the Poynting vectors of the incident and reflected electromagnetic fields. The green line (related to the upper axis) is the intensity profile along $x = 28.8\lambda$. The red line is the Poynting vector profile along the laser axis ($y = 0$). The colorbar is the electron density in logarithmic scale, $\log_{10}(n_e/n_c)$. **c** The temporal evolution of the frequency power spectrum of the EM field is presented in the (ω, t) plane on the logarithmic scale. The black line is the time integrated frequency power spectrum (from the beginning of reflection to the end of the simulation)

(ω, t) plane. The EM field components (in the region in front of the solid surface) are Fourier transformed to the frequency domain along the longitudinal direction and then transversely integrated within the range of $-5 < y(\lambda) < 5$. The high-order harmonics are generated after the reflection with decreasing power. The intensity spectrum falls off according to the power law $I_\omega \approx \omega^{-5/256}$. In our case, the intensity decrease is partially compensated by the focusing effect from the concave mirror, therefore the intensity of the high order harmonics waves on the laser axis becomes comparable to the light at the fundamental frequency ω_0 . The time integrated frequency power spectrum is shown by the black line. It represents the energy partition in the different frequency components.

γ -Ray emission and e^+e^- pair creation. When the high-order harmonic pulse collides with the ultra-relativistic electron bunch, the number of emitted γ -photons significantly increases. Figure 5a shows the γ -photon density distribution (normalized to the critical density) in logarithmic scale at $t = 43T_0$, when the incident laser has been almost completely reflected. The highest photon density appears on both sides of the laser axis ($y = 0$). It is due to the fact that the reflected field is not focused to the center at this position as discussed above and the high-density region is also correlated with the double peak of the transverse intensity amplitude shown in Fig. 4b. The corresponding laser intensity profile along the laser axis is indicated by the red line in Fig. 5a, which contains the high-harmonic components. The green and black lines represent the density profile (normalized to $20n_c$) of photons and electrons on the laser axis, respectively. The peak photon density on the axis reaches $50n_c$ and it even exceeds $300n_c$ on both sides. In the inset of Fig. 5b, the black, green, red, and blue lines are the energy spectra of the γ -photons at $36T_0$, $41T_0$, $42T_0$, and $43T_0$, respectively. The laser reflection begins at about $t = 41T_0$. From this moment onward the number and energy of the photons increase. Since the reflected field interacts with ultra-relativistic electrons, the emitted photon direction are correlated to the electron direction. The angular-energy distribution of photons at $44T_0$ is shown in Fig. 5b. The energy of the photons reaches 1.5 GeV and they are collimated in the forward direction. The transverse emittance of the forward propagating γ -photons is about 2.96 mmmrad and the angular divergence is about $\theta_{\text{div}} \approx 0.38$ rad. In the nonlinear Compton scattering regime, the most radiated photon energy can be estimated as $\varepsilon_\gamma \sim \chi_e \gamma m_e c^2$ ^{210,35}. For a typical accelerated electron with the energy of 2 GeV as seen in Fig. 1c, one obtains photons with energy 1 GeV which is consistent with Fig. 5b. The photon energy is much higher than that from the estimate of linear Compton scattering, which proves the nonlinear Compton scattering dominates the γ -ray emission.

10λ to focus the reflected field to the laser axis. Before that, the transverse intensity distribution has double peaks on both sides of the center axis as depicted by the black line in Fig. 4b, which is the intensity profile in transverse direction and the scale of the amplitude is related to the upper axis. In this case, the laser field is reflected to be counter-propagating to the ultra-relativistic electron bunch while the intensity is also enhanced. This effect greatly increases the probability for γ -ray emission and also for the subsequent pair creation. To present the high-order harmonic generation scenario in detail, the frequency power spectrum with logarithmic scale in the 2D simulation is provided in Fig. 4c in

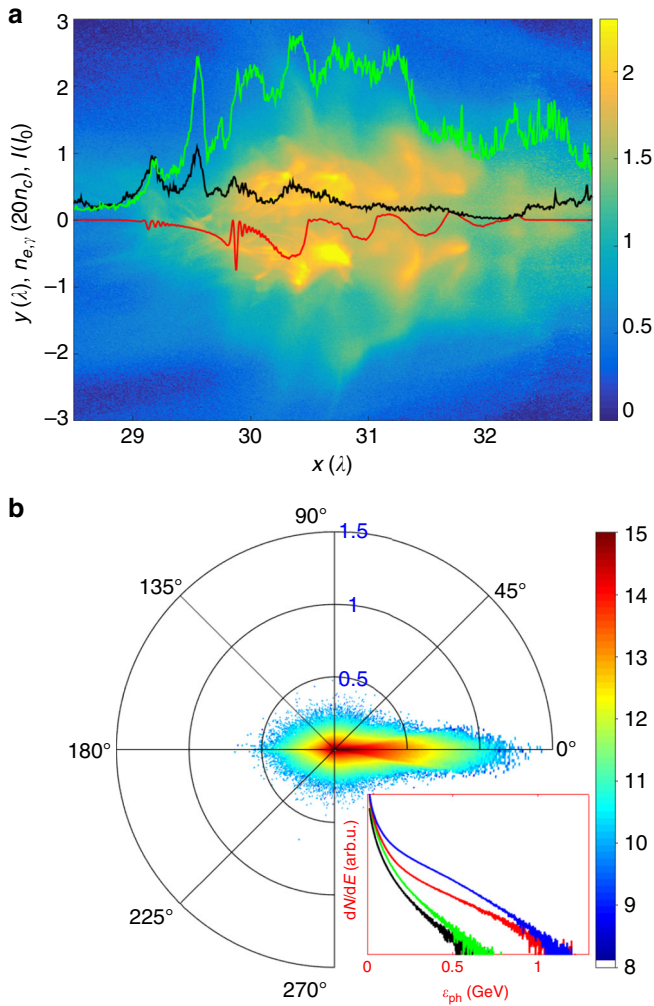


Fig. 5 Gamma-ray generation by reflected field. **a** The photon density distribution at $43T_0$. The black, green and red lines are the profiles of electron density, γ -photon density and EM field intensity along $y = 0$. The colorbar is the photon density in logarithmic scale, $\log_{10}(n_{ph}/n_c)$. **b** The angular-energy distribution of photons at $44T_0$. The colorbar is the number of the photons in logarithmic scale with arbitrary unit. The inset shows the temporal evolution of the photon energy spectrum. The black, green, red, and blue lines represent the time at $36T_0$, $41T_0$, $42T_0$ and $43T_0$, respectively

With the high-energy γ -ray flux, electron-positron pair creation becomes possible via the Breit-Wheeler process^{38,39}. The probability of this QED process is determined by the Lorentz invariant parameter $\chi_\gamma = \sqrt{(F^{\mu\nu}k_\nu)^2}/(E_s m_e c)$ ³⁹, with k_ν the four-momenta of the photon. In the 3-D notation the parameter can be given as

$$\chi_\gamma = (1/E_s) \sqrt{(\hbar\omega_s \mathbf{E}/mc^2 + \mathbf{k}_\gamma \times \mathbf{B}/mc)^2 - (\mathbf{k}_\gamma \cdot \mathbf{E}/mc)^2}$$
⁵⁷. In an EM wave propagating along the x -direction, $\chi_\gamma = (E/E_s)(\hbar\omega - k_x c)/mc^2$, the counter-propagating and co-propagating photons have $\chi_\gamma^{\downarrow} \simeq 2(\hbar\omega/mc^2)(E/E_s)$ and $\chi_\gamma^{\uparrow} \simeq 0$, respectively. Therefore, the reflected high order harmonic EM field provides a relatively large probability for the BW process. The profiles of the positron density, EM field intensity and χ_γ are shown in Fig. 6a with black, red and blue lines, respectively. One finds that the χ_γ has separated peaks

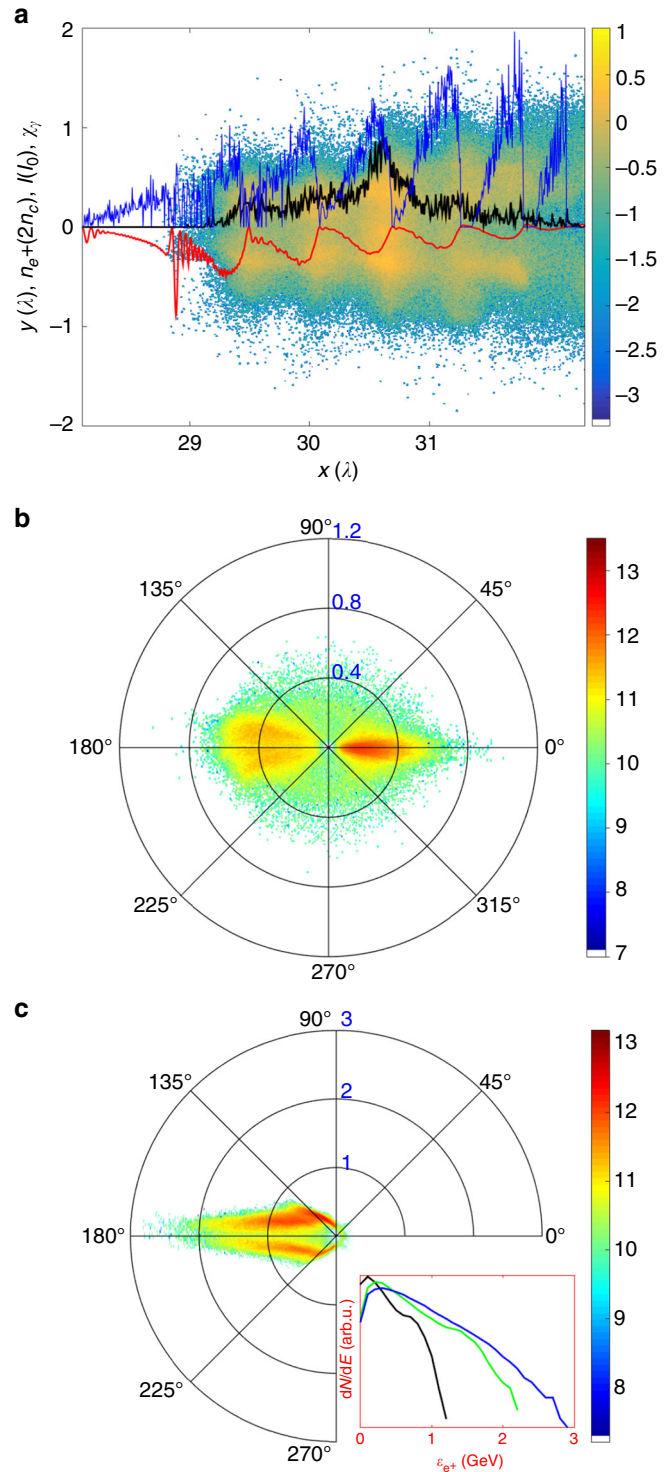


Fig. 6 Electron-positron pair production. **a** The positron density distribution at $44T_0$. The black, red, and blue lines are the profiles of positron density, EM field intensity, and χ_γ along $y = 0$. The colorbar is the positron density in logarithmic scale, $\log_{10}(n_{e^+}/n_c)$. **b, c** are the angular-energy distribution of the generated positrons at $43T_0$ and $57T_0$. The colorbar in **b, c** represent the number of the positrons in logarithmic scale in arbitrary unit. The inset in **c** shows the temporal evolution of the positron energy spectrum. The black, green and blue lines represent the time at $44T_0$, $51T_0$ and $57T_0$, respectively

according to the reflected wave packets which results in the generated positron trains as shown by the positron density distribution. Similar to the γ photons distribution, the highest positron density is located also on both sides of the laser axis. The corresponding angular-energy distributions are shown in Fig. 6b, c. The energy spectra of the positrons shown in the inset of Fig. 6c indicate that the positrons are created and then accelerated by the reflected EM field. At $t = 43T_0$, the positrons are just being created and have the initial directions accompanied with the γ photons. Subsequently the positrons are trapped and accelerated by the reflected EM field in the backward direction. At a later stage ($t = 57T_0$ in (c)), the positrons are further accelerated to the maximum of 3 GeV but are transversely disturbed by the laser field. Therefore the beam quality of the positrons is slightly decreased with a transverse emittance of 32.72 mmmrad and an angular divergence of $\theta_{\text{div}} \approx 2.07$ rad. The forward propagating positrons disappear since they are trapped and co-moving with the reflected pulse. Some of the positrons, which are not trapped, are leaving the simulation box. The positron acceleration regime is similar to the direct laser acceleration of the electrons. Furthermore, the positron generation and acceleration are self-consistent without any extra target design and alignment.

In order to check the robustness of the mechanism, we carried out 3D simulation with the same parameters. The simulation results are presented in Fig. 7. The monochrome stripes are the reflected EM field intensity. The high harmonics spikes can be seen clearly in the region of $20.5 < x(\lambda) < 21.5$. The colorbar is normalized to the incident laser intensity I_0 . The focusing effect is indicated by the deep dark spikes. The colorful cloud in the simulation box shows the density of the γ photons in the 3D volume. The cross-section of the photon density at $x = 22\lambda$ is projected on the y - z plane, which describes the brightness of the γ -ray flux. The total number of the γ -photons is 1.7×10^{12} with the mean energy about 58 MeV. Considering the volume of $1\lambda^3$, the power of the γ -ray flux reaches 0.74PW with the brilliance of $2 \times 10^{24} \text{ s}^{-1} \text{ mm}^{-2} \text{ mrad}^{-2} (0.1\% \text{ BW})^{-1}$ (at 58 MeV). The brilliance as a function of the photon energy is plotted in Fig. 7b. It decreases with the photon energy growing, which is consistent with the energy spectra shown in the inset of Fig. 5b. However, the brilliance is still above 10^{22} with the photon energy of 600 MeV. The black dots in the simulation box represent the generated high energy positrons ($\epsilon_{e^+} > 500$ MeV). The total positron charge, which can be collected in the backward direction, is about 0.9 nC. The energy in the γ -photons is about 15 J and the energy of the pairs is about 0.35 J. The corresponding conversion efficiency from laser to γ -photon is about 1.4% and laser to pairs is about 0.035%.

Discussion

The upcoming laser facilities such as ELI³ will reach the laser intensities of $10^{23-24} \text{ W cm}^{-2}$. At such the intensity the laser-plasma interaction is ultra-relativistic and dominated by the radiation friction force. The ultra-intense EM pulses provide opportunities to investigate strong field QED effects and laboratory astrophysics. The proposed scheme, in which ultra-bright γ -ray flux and GeV positron beams are produced, can be considered as a candidate for potential experiments carried out on such lasers. The well collimated high brilliance γ -ray flux propagates in the direction opposite to the reflected laser wave. It can be easily collected. The high energy e^+e^- pairs are generated and accelerated by a single laser pulse.

In summary, we propose a regime for γ -ray and e^+e^- pair creation via a relativistic oscillating plasma mirror mechanism. The pulse reflected by the mirror experiences a frequency up-shift according to the Doppler effect. The high order harmonics field

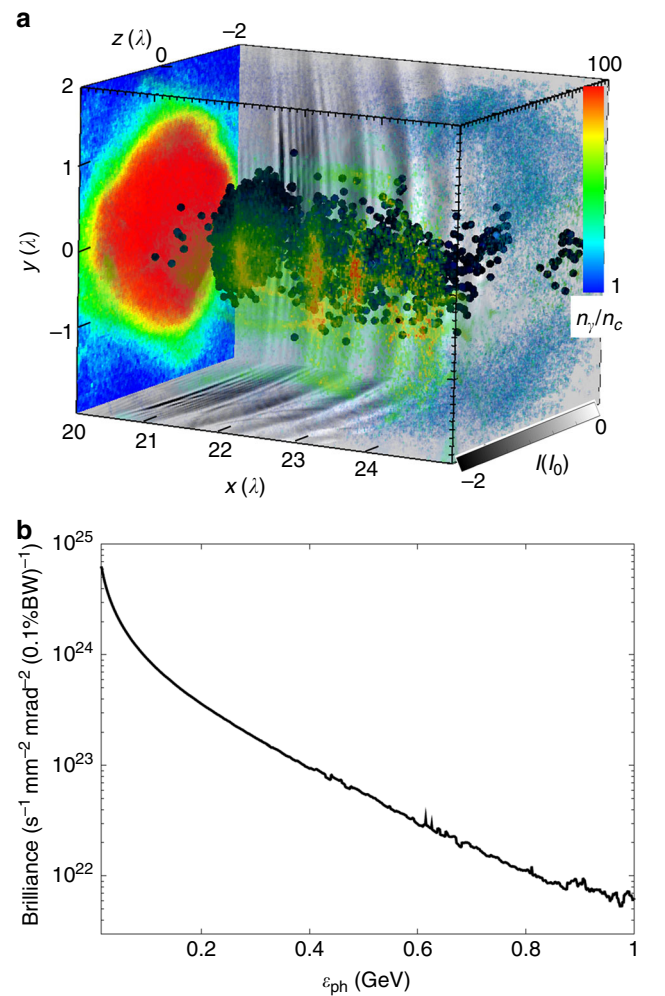


Fig. 7 3D results and gamma-ray brilliance. **a** The monochrome stripes in the bottom (x - z plane) is the projection of the reflected EM (electromagnetic) field intensity distribution on the laser axis ($y = 0$ plane). The corresponding distribution in the $z = 0$ plane is projected in the x - y plane. The colorful cloud shows the γ -photon density distribution in the 3D volume. The photon density cross-section at $x = 22\lambda$ is projected on the y - z plane. The black dots represent the generated positrons with the kinetic energy higher than 500 MeV. The figure is produced based on the 3D simulation results at $t = 57 T_0$. **b** The brilliance of the γ -photon with respect to the photon energy

has the double intensity enhanced due to the focusing and compression effect from the concave deformation of the solid target. The high energy radiation trapped electrons, accelerated by the $\mathbf{j} \times \mathbf{B}$ force, are colliding with the reflected EM field and emit γ photons with high brightness and high energy. The photons are counter-propagating in the intense field which provides a large cross-section for Breit-Wheeler process. A large number of e^+e^- pair are created with the density as high as several critical densities and the total positron charge is of the order of nano-Coulomb.

Methods

Simulation setup. The simulations are performed with the relativistic EM code EPOCH^{58,59} in 2D and 3D cases. QED effects for nonlinear Compton scattering and multiphoton BW process are implemented in the simulations. A Monte-Carlo algorithm is employed for modeling the photon emission and BW process. The local constant field approximation is used to treat the external EM field as a plane wave in the instantaneous rest frame of the charge. The Bremsstrahlung radiation and the e^+e^- annihilation effects are ignored in the

code. For a typical electron with 1 GeV, the radiation stopping power in the overdense hydrogen plasma is about 10 MeV/mm, and is therefore not significant on the distances as short as several tens microns. The linear-polarized laser pulse with the peak intensity of $3 \times 10^{23} \text{ W cm}^{-2}$ incidents from the left boundary and propagates along the x -axis. The simulation box has the size of 40λ and 40λ in the x - and y -direction. The hydrogen plasma layer is in the interval from $x = 10\lambda$ to $x = 32\lambda$. The longitudinal density linearly increases from 0 to $4n_c$ in the interval of $10\lambda < x < 12\lambda$, then it remains constant for 20λ . A solid gold layer is attached to the plasma layer with the density of $600n_c$. It is localized in the region from $x = 32\lambda$ to $x = 33\lambda$. The ionization process is not switched on in the simulations and all the targets are assumed to be pre-ionized. The gold ions are set to be Au^{51+} . The mesh size for the 2D simulation is $\delta x = \delta y = \lambda/200$. The timestep is $0.003T_0$, where T_0 is the laser period. All the quasiparticles (64 per cell) are initially at rest. In the 3D simulation, the box size is $X \times Y \times Z = 25\lambda \times 20\lambda \times 20\lambda$, sampled by $1500 \times 800 \times 800$ cells with 10 quasiparticles per cell.

Data availability

The data that support the plots and findings of this paper are available from the corresponding author upon reasonable request.

Received: 28 March 2018 Accepted: 16 November 2018

Published online: 10 December 2018

References

1. Yanovsky, V. et al. Ultra-high intensity—300-TW laser at 0.1 Hz repetition rate. *Opt. Express* **16**, 2109 (2008).
2. Pirozhkov, A. S. et al. Approaching the diffraction-limited, bandwidth-limited petawatt. *Opt. Express* **25**, 20486 (2017).
3. Mourou, G., Korn, G., Sandner, W. & Collier, J. *Extreme Light Infrastructure (Whitebook)* (THOSS Media GmbH, Berlin, Germany, 2011).
4. Chriaux, G. et al. Apollon-10p: status and implementation. *AIP Conf. Proc.* **1462**, 78 (2012).
5. Mourou, G. A., Tajima, T. & Bulanov, S. V. Optics in the relativistic regime. *Rev. Mod. Phys.* **78**, 309 (2006).
6. Di Piazza, A., Hatsagortsyan, K. Z. & Keitel, C. H. Strong signatures of radiation reaction below the radiation-dominated regime. *Phys. Rev. Lett.* **102**, 254802 (2009).
7. Di Piazza, A., Müller, C., Hatsagortsyan, K. Z. & Keitel, C. H. Extremely high-intensity laser interactions with fundamental quantum systems. *Rev. Mod. Phys.* **84**, 1177 (2012).
8. Bulanov, S. V. Magnetic reconnection: from MHD to QED. *Plasma Phys. Control. Fusion* **59**, 014029 (2017).
9. Bamber, C. et al. Studies of nonlinear qed in collisions of 46.6 GeV electrons with intense laser pulses. *Phys. Rev. D* **60**, 092004 (1999).
10. Bell, A. R. & Kirk, J. G. Possibility of prolific pair production with high-power lasers. *Phys. Rev. Lett.* **101**, 200403 (2008).
11. Sokolov, I. V., Naumova, N. M., Nees, J. A. & Mourou, G. A. Pair creation in qed-strong pulsed laser fields interacting with electron beams. *Phys. Rev. Lett.* **105**, 195005 (2010).
12. Bulanov, S. S., Mur, V. D., Narozhny, N. B., Nees, J. & Popov, V. S. Multiple colliding electromagnetic pulses: a way to lower the threshold of e^+e^- pair production from vacuum. *Phys. Rev. Lett.* **104**, 220404 (2010).
13. Gonoskov, A. A., Korzhimanov, A. V., Kim, A. V., Marklund, M. & Sergeev, A. M. Ultrarelativistic nanoplasmonics as a route towards extreme-intensity attosecond pulses. *Phys. Rev. E* **84**, 046403 (2011).
14. Phuoc, K. Ta et al. All-optical compton gamma-ray source. *Nat. Photonics* **6**, 308 (2012).
15. Nakamura, T. et al. High-power γ -ray flash generation in ultraintense laser-plasma interactions. *Phys. Rev. Lett.* **108**, 195001 (2012).
16. Ridgers, C. P. et al. Dense electron–positron plasmas and ultraintense γ rays from laser-irradiated solids. *Phys. Rev. Lett.* **108**, 165006 (2012).
17. Ji, L. L., Pukhov, A., Kostyukov, I. Y., Shen, B. F. & Aklis, K. Radiation-reaction trapping of electrons in extreme laser fields. *Phys. Rev. Lett.* **112**, 145003 (2014).
18. Blackburn, T. G., Ridgers, C. P., Kirk, J. G. & Bell, A. R. Quantum radiation reaction in laser–electron-beam collisions. *Phys. Rev. Lett.* **112**, 015001 (2014).
19. Zhu, X.-L. et al. Enhanced electron trapping and γ ray emission by ultra-intense laser irradiating a near-critical-density plasma filled gold cone. *New J. Phys.* **17**, 053039 (2015).
20. Ribeyre, X. et al. Pair creation in collision of γ -ray beams produced with high-intensity lasers. *Phys. Rev. E* **93**, 013201 (2016).
21. Gu, Y. J., Klimo, O., Weber, S. & Korn, G. High density ultrashort relativistic positron beam generation by laser–plasma interaction. *New J. Phys.* **18**, 113023 (2016).
22. Li, H.-Z. et al. Ultra-bright gamma-ray emission and dense positron production from two laser-driven colliding foils. *Sci. Rep.* **7**, 17312 (2017).
23. Chang, H. X. et al. Brilliant petawatt gamma-ray pulse generation in quantum electrodynamic laser–plasma interaction. *Sci. Rep.* **7**, 45031 (2017).
24. Zhu, X.-L. et al. Dense GeV electron–positron pairs generated by lasers in near-critical-density plasmas. *Nat. Commun.* **7**, 13686 (2016).
25. Gong, Z. et al. Brilliant GeV gamma-ray flash from inverse compton scattering in the QED regime. *Plasma Phys. Control. Fusion* **60**, 044004 (2018).
26. Vranic, M., Klimo, O., Weber, S. & Korn, G. Multi-GeV electron–positron beam generation from laser–electron scattering. *Sci. Rep.* **8**, 4702 (2018).
27. Blackburn, T. G. & Marklund, M. Nonlinear Breit-Wheeler pair creation with bremsstrahlung γ rays. *Plasma Phys. Control. Fusion* **60**, 054009 (2018).
28. Galy, J., Maucec, M., Hamilton, D. J., Edwards, R. & Magill, J. Bremsstrahlung production with high-intensity laser matter interactions and applications. *New J. Phys.* **9**, 23 (2007).
29. Ledingham, K. W. D. & Galster, W. Laser-driven particle and photon beams and some applications. *New J. Phys.* **12**, 045005 (2010).
30. Giulietti, A. et al. Intense γ -ray source in the giant-dipole-resonance driven by 10-TW laser pulses. *Phys. Rev. Lett.* **101**, 105002 (2008).
31. Sarri, G. et al. Ultrahigh brilliance multi-MeV γ -ray beams from nonlinear relativistic Thomson scattering. *Phys. Rev. Lett.* **113**, 224801 (2014).
32. Stark, D. J., Toncian, T. & Arefiev, A. V. Enhanced multi-MeV photon emission by a laser-driven electron beam in a self-generated magnetic field. *Phys. Rev. Lett.* **116**, 185003 (2016).
33. Bula, C. et al. Observation of nonlinear effects in compton scattering. *Phys. Rev. Lett.* **76**, 3116 (1996).
34. Di Piazza, A., Hatsagortsyan, K. Z. & Keitel, C. H. Quantum radiation reaction effects in multiphoton compton scattering. *Phys. Rev. Lett.* **105**, 220403 (2010).
35. Benedetti, A., Tamburini, M. & Keitel, C. H. Giant collimated gamma-ray flashes. *Nat. Photon.* **12**, 319 (2018).
36. Cipiccia, S. et al. Gamma-rays from harmonically resonant betatron oscillations in a plasma wake. *Nat. Phys.* **7**, 867 (2011).
37. Zhu, X. L. et al. Bright attosecond γ -ray pulses from nonlinear Compton scattering with laser-illuminated compound targets. *Appl. Phys. Lett.* **112**, 174102 (2018).
38. Breit, G. & Wheeler, J. A. Collision of two light quanta. *Phys. Rev.* **46**, 1087 (1934).
39. Nikishov, A. I. & Ritus, V. I. Interaction of electrons and photons with a very strong electromagnetic field. *Sov. Phys. Uspekhi* **13**, 303 (1970).
40. Gelfer, E. G. et al. Optimized multibeam configuration for observation of QED cascades. *Phys. Rev. A* **92**, 022113 (2015).
41. Jirka, M. et al. Electron dynamics and γ and e^+e^- production by colliding laser pulses. *Phys. Rev. E* **93**, 023207 (2016).
42. Tamburini, M., Piazza, A., Di & Keitel, C. H. Laser-pulse-shape control of seeded QED cascades. *Sci. Rep.* **7**, 5694 (2017).
43. Gu, Y. J. & Weber, S. Intense, directional and tunable γ -ray emission via relativistic oscillating plasma mirror. *Opt. Express* **26**, 19932 (2018).
44. Max, C. E., Arons, J. & Langdon, A. B. Self-modulation and self-focusing of electromagnetic waves in plasmas. *Phys. Rev. Lett.* **33**, 209 (1974).
45. Gu, Y. J. et al. Laser guiding plasma channel formation criterion in highly relativistic regime. *Appl. Phys. Lett.* **99**, 241501 (2011).
46. Schwinger, J. On gauge invariance and vacuum polarization. *Phys. Rev.* **82**, 664 (1951).
47. Corde, S. et al. Femtosecond X rays from laser–plasma accelerators. *Rev. Mod. Phys.* **85**, 1 (2013).
48. Liu, B. et al. Generating overcritical dense relativistic electron beam via self-matching resonance acceleration. *Phys. Rev. Lett.* **110**, 045002 (2013).
49. Wang, H. Y., Liu, B., Yan, X. Q. & Zepf, M. Gamma-ray emission in near critical density plasmas at laser intensities of 10^{21} W/cm^2 . *Phys. Plasmas* **22**, 033102 (2015).
50. Schlegel, T. et al. Relativistic laser piston model: ponderomotive ion acceleration in dense plasmas using ultraintense laser pulses. *Phys. Plasmas* **16**, 083103 (2009).
51. Bulanov, S. V., Naumova, N. M. & Pegoraro, F. Interaction of an ultrashort, relativistically strong laser pulse with an overdense plasma. *Phys. Plasmas* **1**, 745 (1994).
52. Lichters, R., Meyer-ter-Vehn, J. & Pukhov, A. Short pulse laser harmonics from oscillating plasma surfaces driven at relativistic intensity. *Phys. Plasmas* **3**, 3425 (1996).
53. Vincenti, H. et al. Optical properties of relativistic plasma mirrors. *Nat. Commun.* **5**, 3403 (2014).
54. Bulanov, S. V., Esirkepov, T. Z., Kando, M. & Koga, J. Relativistic mirrors in laser plasmas (analytical methods). *Plasma Sources Sci. Technol.* **25**, 053001 (2016).
55. Naumova, N. M., Nees, J. A., Sokolov, I. V., Hou, B. & Mourou, G. A. Relativistic generation of isolated attosecond pulses in a λ^3 focal volume. *Phys. Rev. Lett.* **92**, 063902 (2004).

56. Gordienko, S., Pukhov, A., Shorokhov, O. & Baeva, T. Relativistic Doppler effect: universal spectra and zeptosecond pulses. *Phys. Rev. Lett.* **93**, 115002 (2004).
57. Bulanov, S. S., Schroeder, C. B., Esarey, E. & Leemans, W. P. Electromagnetic cascade in high-energy electron, positron, and photon interactions with intense laser pulses. *Phys. Rev. A* **87**, 062110 (2013).
58. Ridgers, C. et al. Modelling gamma-ray photon emission and pair production in high-intensity laser–matter interactions. *J. Comput. Phys.* **260**, 273 (2014).
59. Arber, T. D. et al. Contemporary particle-in-cell approach to laser-plasma modelling. *Plasma Phys. Control. Fusion* **57**, 113001 (2015).

Acknowledgments

This work was supported by the project ELITAS (CZ.02.1.01/0.0/0.0/16_013/0001793) and by the project High Field Initiative (CZ.02.1.01/0.0/0.0/15_003/0000449) both from European Regional Development Fund. It is also supported by the project ADONIS (Advanced research using high intensity laser produced photons and particles), CZ.02.1.01/0.0/0.0/16_019/0000789, from European Regional Development Fund. The support of Czech Science Foundation is acknowledged (Project No. 18-09560S, O.K.). Computational resources were provided by the MetaCentrum under the program LM2010005, IT4Innovations Centre of Excellence under projects CZ.1.05/1.1.00/02.0070 and LM2011033 and by ECLIPSE cluster of ELI-Beamlines. The EPOCH code was developed as part of the UK EPSRC funded projects EP/G054940/1.

Author contributions

Y.J. Gu carried out the simulations, analyzed the results, generated the figures, and wrote the bulk of the manuscript. O. Klimo, S. Bulanov, and S. Weber discussed the physics and

interpreted the results of the simulations. All authors contributed to the preparation of the manuscript.

Additional information

Competing interests: The authors declare no competing interests.

Reprints and permission information is available online at <http://npg.nature.com/reprintsandpermissions/>

Publisher's note: Springer Nature remains neutral with regard to jurisdictional claims in published maps and institutional affiliations.



Open Access This article is licensed under a Creative Commons Attribution 4.0 International License, which permits use, sharing, adaptation, distribution and reproduction in any medium or format, as long as you give appropriate credit to the original author(s) and the source, provide a link to the Creative Commons license, and indicate if changes were made. The images or other third party material in this article are included in the article's Creative Commons license, unless indicated otherwise in a credit line to the material. If material is not included in the article's Creative Commons license and your intended use is not permitted by statutory regulation or exceeds the permitted use, you will need to obtain permission directly from the copyright holder. To view a copy of this license, visit <http://creativecommons.org/licenses/by/4.0/>.

© The Author(s) 2018